NANO LETTERS

pubs.acs.org/NanoLett Letter

Tracking Photothermal Heat Generation in ITO Nanocrystals and Its Dissipation to Their Surrounding Environment

Boxi Li,[‖] Xiaobing Chen,[‖] Tanner A. Wilcoxson, Jiho Kang, Thomas M. Truskett,* Delia J. Milliron,* Carlos R. Baiz,* and Sean T. Roberts*

Cite This: https://doi.org/10.1021/acs.nanolett.5c02441 Read Online

ACCESS | Metrics & More | Article Recommendations | Supporting Information

ABSTRACT: Plasmonic metal oxide nanocrystals can readily transduce infrared light into heat for applications in catalysis, therapeutics, and soft robotics. Here, we investigate photothermal pathways in oleate-capped tin-doped indium oxide (ITO) nanocrystals dispersed in toluene, mapping heat transfer dynamics from the ITO lattice to its surface and surrounding solvent. Using rhodamine B dyes adhered to nanocrystal surfaces and toluene as temperature probes, we track photothermal heat dissipation via transient absorption spectroscopy. We find heat transfer from ITO nanocrystals to surface-adsorbed molecules unfolds over tens of picoseconds, followed by heat dissipation into the surrounding solvent over hundreds of picoseconds. We have developed a theoretical model that quantitatively reproduces these kinetics and identifies nanocrystal surface-to-solvent heat transfer as the primary bottleneck in heat dissipation. These insights advance our understanding of nanoscale heat transport involving ITO nanocrystals and offer insights into how to design these materials for heat-driven applications.

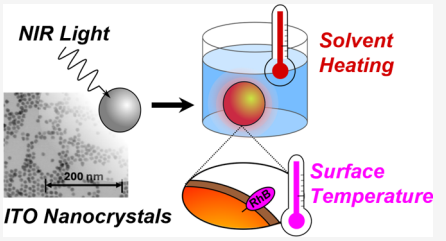

KEYWORDS: *Semiconductor plasmonics, Localized surface plasmon resonance, Near-infrared photoinduced heating, Heat dissipation, Thermal transport, Ultrafast transient absorption spectroscopy*

Downloaded via UNIV OF TEXAS AT AUSTIN on July 25, 2025 at 14:19:16 (UTC).
See https://pubs.acs.org/sharingguidelines for options on how to legitimately share published articles.

Plasmonic metal nanoparticles can readily transduce light into heat. Photothermal devices based on these structures hold potential for several applications, including heat-driven catalysis,[1−3] tumor therapy,[4−6] and nanorobot actuation.[7−9] Shining light on a metal nanoparticle can drive a localized surface plasmon resonance (LSPR) whose properties depend on the nanoparticle's size, shape, composition, and surface ligands.[10−14] Mechanisms that lead to heat generation following LSPR excitation have been established.[15−17] LSPRs dissipate via electron−electron scattering, yielding hot electrons that, on the picosecond time scale, transfer energy to a nanoparticle's lattice via electron−phonon interactions, generating heat.[18,19] Over picosecond-to-nanosecond time scales, this heat dissipates into the surrounding medium[20,21] and factors such as particle size, shape, and concentration have been shown to impact a nanoparticle's ability to raise the temperature of its surroundings.[5,22−25]

Extensive research has focused on heat generation in plasmonic systems composed of noble metals and metal chalcogenides such as Au, Ag, and $Cu_{2-x}Se$.[3,16,26−30] More recently, degenerately doped colloidal metal oxides have gained attention due to their compositionally and electrically tunable LSPRs, making them versatile for photothermal applications driven by near-IR (NIR) or mid-IR (MIR) excitation.[23,31−34] This includes reshaping the structure of nanocrystal (NC) assemblies held together by temperature-responsive frameworks for use in infrared photonics.[35−38] Among metal oxides, tin-doped indium oxide (ITO) NCs[10,12,39] are particularly appealing for biorelated applications as their LSPRs can be tuned to fall within the NIR transmission window of biological tissue.[40,41] While photoexcited dynamics within nanofabricated ITO structures have received some attention,[42−44] photoinduced heating of colloidal ITO NCs remains underexplored.[39,45−49] Moreover, to our knowledge no studies have quantified heat transfer from plasmonic particles to their surroundings, whether they be metals or metal oxides, by simultaneously probing molecules situated at different distances from a particle's surface.

In this work, we address this knowledge gap by using transient absorption (TA) spectroscopy to directly track heat transfer from plasmonic ITO NCs to molecules at their surfaces (ligands and near-surface solvent) and energy transfer from this surface layer into the surrounding solvent. In parallel, we employ a two-interface model that couples the ITO NC lattice, surface layer, and bulk solvent temperatures in series via two interfacial conductances.[50] We find this model quantitatively reproduces spectroscopic changes captured in TA measurements that stem from LSPR photoexcitation, which has allowed us to identify heat flow from molecules at ITO NC

Received: May 1, 2025
Revised: July 5, 2025
Accepted: July 18, 2025

ACS Publications © XXXX American Chemical Society

surfaces to the surrounding solvent as a primary bottleneck in heat dissipation. Our study introduces general experimental and theoretical approaches to describe heat dissipation within plasmonic systems, providing a step toward using NCs for NIR photothermal applications.

Scheme 1 provides an overview of the photothermal process we investigate and the spectroscopic probes used to track heat dissipation from ITO NCs. Oleate-capped ITO NCs were synthesized via a modified slow-injection method and dispersed in toluene after multiple washings to remove unbound oleate ligands.[51] To quantify the ITO NC surface temperature following photoexcitation, we adsorbed Rhodamine B (RhB), a dye molecule whose optical absorption spectrum shifts with temperature, onto ITO NCs. This enabled detection of kinetics governing heat flow into and out of the surface layer (SL) of molecules in direct contact with ITO by tracking absorption changes of RhB probe molecules following LSPR excitation by a femtosecond NIR pulse (Scheme 1, magenta arrow). Note, the fraction of RhB in the surface layer is much smaller than that of oleate (Supporting Information, Section S2.2), supporting its use as a nonperturbative temperature reporter. The subsequent heat transfer into the bulk solvent was tracked by monitoring temperature-dependent changes in the absorption spectrum of toluene vibrational modes in the MIR spectral range (Scheme 1, green arrow). Sample preparation, TA instrumentation, data collection, analysis, and modeling methods can be found in Supporting Information Sections S1−S4.

Scheme 1. Illustration of Thermal Relaxation Pathway Interrogated Here for ITO NCs (Blue Sphere) Following Photoexcitation by a NIR Pulse[a]

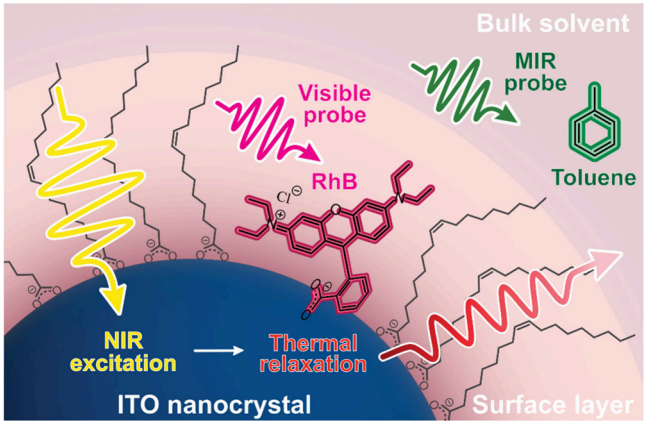

[a]Hot electrons generated by the pulse transfer their energy to the ITO NC lattice, which in turn passes it to the solvent through a surface layer of molecules at the NC surface. RhB dye molecules adsorbed onto the ITO surface (magenta), probed using visible light, report on the temperature of the surface layer. Vibrational modes of the solvent, toluene (green), probed using MIR light, report on heat transfer from the surface layer to the bulk solvent.

The average diameter of the ITO NCs we employ was characterized using both solution-phase small-angle X-ray scattering (SAXS) and bright-field scanning transmission electron microscopy (STEM), which return similar values of 10.5 ± 1.1 nm and 9.9 ± 1.0 nm, respectively (Figure 1A). The NC's Sn dopant concentration was determined to be 4.6 at. % via Inductively Coupled Plasma-Optical Emission Spectrometry (ICP-OES) of digested NCs. The ITO NC absorption spectrum (Figure 1B) shows two prominent features: an LSPR peak centered near 2100 nm and the onset of ITO's bandgap below 400 nm. After RhB functionalization, these features remain unchanged, but an additional set of vibronic peaks associated with RhB's S_1 state appears between 500 and 600 nm (Figure 1B, inset).

To assess the ability of RhB and toluene to serve as local temperature probes, their steady-state absorption spectra were collected at varying temperatures (Figures 1C and 1D). To account for changes in RhB's absorption profile upon binding to ITO, steady-state absorption spectra of RhB with increasing temperature were collected for a RhB-functionalized ITO NC thin film deposited on a quartz substrate. Use of a thin film over a NC suspension ensures all RhB molecules in the sample are in contact with ITO rather than existing in equilibrium between adsorption on ITO and desorption into the solvent.[3] Difference spectra, computed by subtracting RhB's absorption spectrum measured at 25 °C from its absorption at elevated temperature (Figure 1C), show decreasing absorbance around 525 and 550 nm and an absorption gain around 580 nm with increasing temperature, consistent with prior reports.[3,52] Similar analysis was conducted for absorption spectra of an ITO NC dispersion in toluene (Figure 1D). As temperature increases, the toluene band near 1460 cm^{-1}, which corresponds to C−H bending of toluene's methyl group (B_1) and hexene ring (B_2),[53,54] decreases linearly (Figure S2.1). This absorption decrease with rising temperature is also seen for neat toluene in the absence of ITO (Figure S2.2).

Picosecond-to-nanosecond dynamics of RhB molecules at the surface of photoexcited ITO NCs were tracked by pumping the LSPR with a 2000 nm pulse and probing the absorption of RhB with a visible pulse. TA spectra of ITO NCs and a RhB-ITO suspension in toluene were compared, which highlights spectral features between 500−600 nm assigned to RhB (Figure 2A). TA spectra of both ITO NCs and RhB-ITO exhibit a broad photoinduced absorption (PIA) that extends into the short wavelength region below 400 nm. This feature arises from a reversal of the Burstein−Moss shift due to heating of electrons in ITO's conduction band following LSPR dissipation, along with changes in ITO's dielectric function caused by electron and lattice heating.[39]

TA spectral features stemming from RhB were isolated by subtracting ITO TA spectra (Figure 2A, dashed lines) from RhB-ITO spectra (Figure 2A, solid lines). The resulting TA difference spectra recorded at a fluence of 1.1 mJ/cm^2 are showcased in Figure 2B. In addition to a negative ground state bleach (GSB) seen at 555 nm at all delay times, two RhB-specific features are observed: a PIA band at 425 nm at short delays, which decays over a few picoseconds, and a PIA at 580 nm that rises over a few picoseconds and decays over longer time delays. The latter feature is assigned to heating of RhB, as benchmarked by comparison to temperature difference spectra computed by subtracting steady-state absorption spectra of RhB measured at 52 and 25 °C (Figure 2C, bottom).

The PIA feature at 425 nm observed at short time delays, however, is not expected to arise from RhB heating. Previous studies investigating plasmonic F- and In-co-doped CdO (FICO) metal oxide NCs[55] and ITO NCs[49] in contact with RhB have observed a similar PIA feature stemming from the transfer of hot electrons generated by plasmonic excitation to RhB, forming the RhB anion. A comparison of the reported RhB anion TA spectrum[55,56] and the TA spectrum at 1 ps shows agreement (Figure 2C, top), indicating the 425 nm

https://doi.org/10.1021/acs.nanolett.5c02441
Nano Lett. XXXX, XXX, XXX−XXX

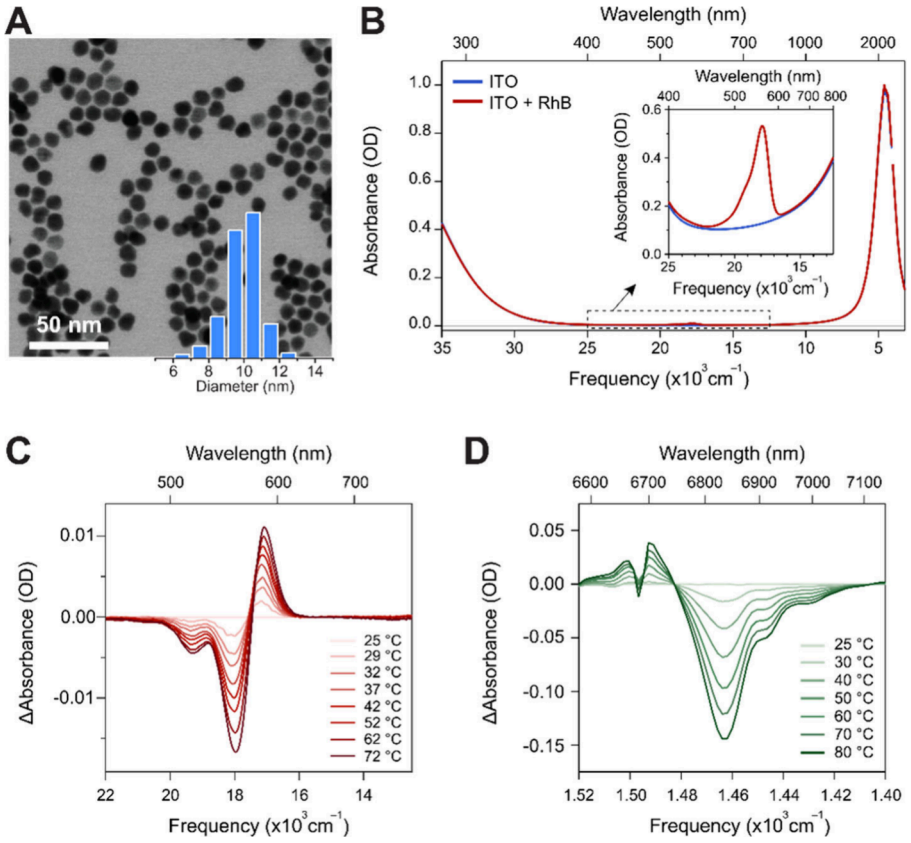

Figure 1. (A) SEM image of ITO NCs. The inset bar plot highlights their size distribution determined via STEM size analysis. (B) Steady-state absorption spectra of 0.01 vol.% ITO NCs in toluene before (blue) and after RhB functionalization (0.89 μM RhB, red). Inset: Visible absorption spectra of 0.4 vol% ITO (blue) and RhB-functionalized ITO (40 μM RhB, red), which are the samples used for TA experiments to enhance the visible response. (C) Temperature-dependent changes in the absorbance of a RhB-ITO NC film. Difference spectra were obtained by subtracting the absorption spectrum measured at 25 °C from spectra recorded at higher temperatures. (D) Temperature-dependent changes of the MIR absorption spectrum of toluene. Difference spectra are calculated relative to a spectrum taken at 25 °C.

band arises from hot electron transfer from ITO to RhB. This assignment is supported by recent fluence-dependent ultrafast measurements of ITO NCs,[49] which concluded that sufficiently hot electrons can transfer from ITO to RhB given the energy alignment of RhB's LUMO orbital and ITO's conduction band (Supporting Information, Section S3.3). Following hot electron transfer, electrons can transfer back to ITO, leading to the loss of the 425 nm PIA band.

As the 580 nm PIA band for RhB heating grows within the first few picoseconds after photoexcitation, which coincides with the decay of the RhB anion, it may be natural to assume the anion decay is responsible for RhB heating. However, fluence-dependent TA spectra reveal the dominant heating pathway is heat transfer from the ITO lattice following electron−lattice equilibration rather than electron transfer from anions. Lowering the excitation fluence, which lowers the initial temperature of the hot electron distribution generated by the pump, fully suppresses hot electron transfer (Supporting Information, Section S3.3), yet the 580 nm PIA band due to RhB heating is clearly seen at all fluences we report (Figure 2D), indicating RhB is heated by mechanisms apart from anion recombination. We also note prior estimates of the RhB anion yield upon photon absorption by ITO[49] and FICO NCs[55] found hot electron transfer occurs with a quantum yield of only ∼1−1.4%, meaning most of the excitation pulse energy drives NC lattice heating. As this heat will dissipate through a NC's surface, impacting all RhB molecules adsorbed to it rather than just a small subset of molecules that accept hot electrons, heat transfer from the ITO lattice to surface-adsorbed RhB is likely the primary mechanism leading to RhB heating.

Kinetic traces tracking photoinduced heating of RhB are plotted for TA spectra measured at different excitation fluences in Figure 2D. As the pump fluence increases from 0.23 to 1.1 mJ/cm^2, the RhB PIA grows linearly in amplitude, but appears to saturate at fluences above 1.1 mJ/cm^2. This is consistent with steady-state absorption spectra of RhB, which show a logarithmic absorption growth at 580 nm with increasing temperature (Figure S2.3). Thus, as NCs are heated further above room temperature, we expect to observe incrementally smaller changes in the magnitude of TA features due to photoinduced heating.

The traces were fit to a multiexponential model (Figure 2D) with three distinct components: a fast rise (a few picoseconds), a slow rise (tens of picoseconds), and a slow decay (a few nanoseconds). Table 1 summarizes the fitted time constants. The fast rise can originate from RhB anion decay, as the GSB of the RhB anion overlaps with the 580 nm PIA associated with RhB heating. Thus, as the RhB anion decays, the PIA signal tracking RhB heating will show a rise even though the anion decay itself does not substantially contribute to photoinduced heating. As the RhB anion is not formed at low fluence, we do not observe this fast rise for the lowest fluences we probe. We assign the slow rise of the signal over tens of picoseconds to heat transfer from the ITO lattice to its

https://doi.org/10.1021/acs.nanolett.5c02441
Nano Lett. XXXX, XXX, XXX−XXX

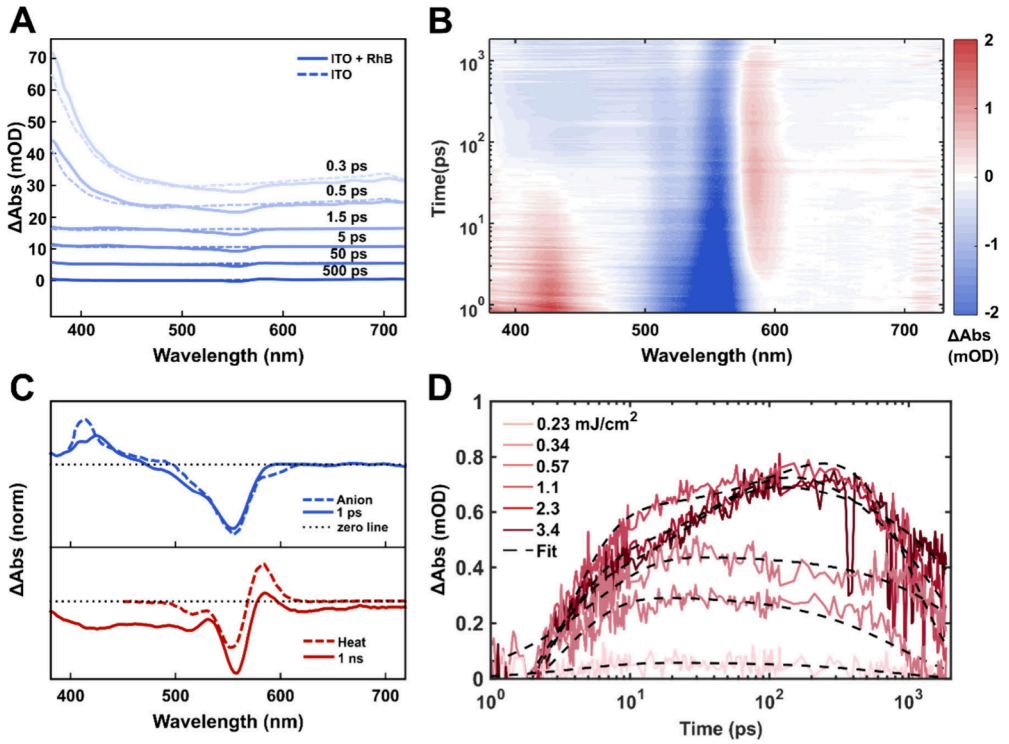

Figure 2. (A) TA spectra of ITO NCs with (solid lines) and without RhB (dotted lines) in toluene measured using a 2000 nm pump pulse with an excitation fluence of 1.1 mJ/cm^2. Spectra measured at different delay times are offset by 5 mOD from early (light blue) to later times (dark blue) for clarity. (B) TA difference spectra highlighting transient features that arise from RhB. Difference spectra were obtained by subtracting ITO TA spectra from RhB-ITO TA spectra. The negative signal at 555 nm corresponds to the RhB GSB. A fast-decaying PIA is observed at 425 nm, while a second PIA at 580 nm grows over tens of picoseconds. (C) Top: comparison of the RhB TA line shape at a 1 ps time delay (solid blue line) with the TA spectrum of the RhB anion (dashed blue line) reported previously.[55,56] Bottom: comparison of the RhB TA line shape at a 1 ns time delay (solid red line) with the temperature difference spectrum obtained by subtracting steady-state absorption spectra of RhB measured at 52 and 25 °C (dashed red line). (D) TA Kinetic traces measured at a probe wavelength of 580 nm that track the strength of the PIA band attributed to RhB heating as a function of pump fluence (light to dark red). Multiexponential fits of these traces are shown as dotted black lines.

Table 1. Exponential Time Constants Used to Fit the Rise and Decay of the RhB TA Signal at 580 nm Measured at Different Excitation Fluences[a]

Fluence (mJ/cm^2)	0.23	0.34	0.57	1.1	2.3	3.4
τ_1 (ps) (Rise)			1.6 ± 0.5	2.5	2.5 ± 0.4	1.9 ± 0.6
τ_2 (ps) (Rise)	4.2 ± 2.5	5.4 ± 0.6	11 ± 7	76	50 ± 19	30 ± 14
τ_3 (ns) (Decay)	0.76 ± 0.31	3.0 ± 0.4	0.78 ± 0.10	1.1	1.6 ± 0.2	3.0 ± 0.7

[a]Error bars are not included for data recorded at a fluence of 1.1 mJ/cm^2 due to a constraint placed on the fit (See Supporting Information, Section S3.4 and Table S3.1).

SL, and the slow decay to heat dissipation out of the SL and into the bulk solvent.

Heat dissipation into the solvent is directly measured by pumping the LSPR with a 2000 nm pulse and tracking photoinduced changes in the vibrational spectrum of toluene using a MIR probe pulse. Figure 3 plots a representative toluene TA spectrum recorded using an excitation fluence of 2.9 mJ/cm^2. Spectra collected with different excitation fluences show similar line shape changes (Figure S3.6). During the first few picoseconds after photoexcitation, we observe a strong positive signal stemming from toluene's C−H bending modes near 1460 cm^{-1} (Figure 3A, green). We attribute this positive signal to increased absorption due to coupling of these modes to the photoexcited LSPR, which can generate a large electric field at an ITO NC's surface, leading to either enhanced absorption or induced transparency of molecules near the surface.[57−61]

After a few picoseconds, the enhanced absorption of toluene's C−H bending modes gives way to a decrease in absorptivity that continues to grow over hundreds of picoseconds (Figure 3A). This observation is consistent with steady-state absorption spectra of toluene, which decrease in amplitude at 1460 cm^{-1} upon heating (Figure 3B), suggesting the MIR TA signal tracks heat dissipation from ITO to toluene. To determine a time scale associated with toluene heating, we averaged the TA signal over the C−H bending line shape (1450−1470 cm^{-1}) and fit it to a biexponential function (Figure 3C). Table 2 summarizes the extracted time constants, which show a fast component (~1 ps) and a slow component (~550 ps), whose values are independent of fluence within measurement uncertainty. In addition to the decay of plasmon-enhanced absorption signal, the fast component may also stem from rapid heating of toluene molecules adsorbed in the NC SL. We assign the slow component to heating of the solvent surrounding ITO NCs.

https://doi.org/10.1021/acs.nanolett.5c02441
Nano Lett. XXXX, XXX, XXX−XXX

Table 2. Biexponential Time Constants for Fits to MIR TA Spectra Tracking Photoinduced Heating of Toluene (Figure 3C)[a]

Fluence (mJ/cm^2)	1.6	1.9	2.4	2.9
τ_1 (ps)	0.84 ± 0.10	0.61 ± 0.23	1.48 ± 0.73	0.49 ± 0.10
τ_2 (ps)	570 ± 85	474 ± 63	561 ± 143	576 ± 39

[a]TA data were spectrally averaged from 1450 to 1470 cm^{-1} prior to fitting. Full fit parameters are given in Table S3.2 of the Supporting Information. Error bars are extracted from the confidence intervals of the fits.

Our TA measurements have allowed us to empirically map photothermal heat dissipation across two interfaces in photoexcited oleate-capped ITO NCs: from the ITO lattice to the SL and from the SL to the bulk solvent. Theoretical modeling serves to quantify the heat conductance and temperature profiles at these interfaces. A recent TA study of photoinduced electron transfer from ITO NCs to surface-adsorbed RhB in hexane accounted for heat transfer to RhB but neglected heat transfer from RhB to its surrounding environment.[49] A second study on heat dissipation through a CdSe NC:oleic acid ligand:CCl_4 bulk solvent interface modeled these three regions by coupling them in series via two interfacial conductances.[50] Building on this approach, we adapted the two-interface model to enable direct comparison with TA signals tracking RhB and toluene photoinduced heating. The modified heat dissipation model, along with the temperature-to-signal interconversions for toluene and RhB, is detailed in Supporting Information Sections S4.1−S4.4. Model parameters, including NC-SL and SL-bulk interfacial conductances (G_{ls} and G_{sb} respectively), SL thickness, and ligand grafting density, were determined through a unified fit to experimental TA spectra tracking toluene photoinduced heating across all investigated fluences (Figure 4A green points/line and Figure S4.2).

G_{ls} and G_{sb} were fit as 96 ± 33 MW/m^{2}K and 3.7 ± 0.1 MW/m^{2}K, respectively, indicating that heat transfer is significantly limited at the SL-bulk interface. The larger error in determining G_{ls} arises as we fit our data to time delays greater than 12 ps to exclude TA signal contributions from toluene's LSPR-enhanced absorption. Despite this error, our fitted conductances closely approximate those reported for oleic acid-capped CdSe NCs in CCl_4 ($G_{ls} \approx 100$ MW/m^{2}K and $G_{sb} \approx 7.5$ MW/m^{2}K), where the SL-bulk interface was also identified as a bottleneck for heat dissipation.[50] Literature on heat dissipation from noble metal nanoparticles and CdSe nanoplatelets mediated by surface ligands have shown that bonding interactions between the ligands and nanoparticles act to enhance heat dissipation relative to that achieved without intermediary ligands.[62−67] Further, both the chemical structure of the ligands' terminal group[65,68] and its degree of interaction with the solvent[69,70] have been found to influence heat transfer to a nanoparticle's surroundings. Sensitivity to specific ligand-solvent interactions may explain why the G_{sb} we obtain for the oleic acid-toluene interface (3.7 MW/m^{2}K) is only half that reported for the oleic acid-CCl_4 interface (~7.5 MW/m^{2}K).[50] Additional parameters recovered from the model show good agreement with literature values: the SL width was fit to 1.5 ± 0.1 nm, consistent with the reported 1−2 nm range of oleic acid extension from the NC surface,[11] while the ligand surface density was fit to 2.4 ± 0.2 oleates/nm,[2] which falls near the reported surface coverage of 3.3 oleates/nm^2 in a recent ITO NC study where ligand coverage was determined by thermogravimetric analysis.[10]

The fitted G_{ls} and G_{sb} correspond to SL heating and cooling time constants of 37 ± 13 ps and 574 ± 16 ps, respectively, roughly aligning with the RhB PIA slow rise and decay (τ_2 and τ_3 in Table 1). Such alignment suggests that fitting solely to the toluene heating data captures the kinetics of RhB heating and cooling in the SL. Indeed, RhB PIA predictions derived from SL temperature evolution in the toluene-fitted model show great agreement with RhB experimental TA kinetics (Figure 4A red points/line and Figure S4.3) giving us further confidence in the value we determine for G_{ls}. The strong overlap between RhB and toluene heating kinetic traces from 10 to ~ 50 ps indicates both are heated within the SL on this time scale, explaining why the toluene fit can determine the NC-SL interfacial conductance.

The temperatures predicted by the fitted two-interface model at three different times following LSPR photoexcitation are visualized in Figure 4B, with yellow indicating the coolest areas and dark red the hottest. By 1 ps, the ITO lattice undergoes rapid thermalization, reaching several hundred degrees above room temperature. Around 50 ps, the NC reaches a quasi-equilibrium with the SL before heat transfer to

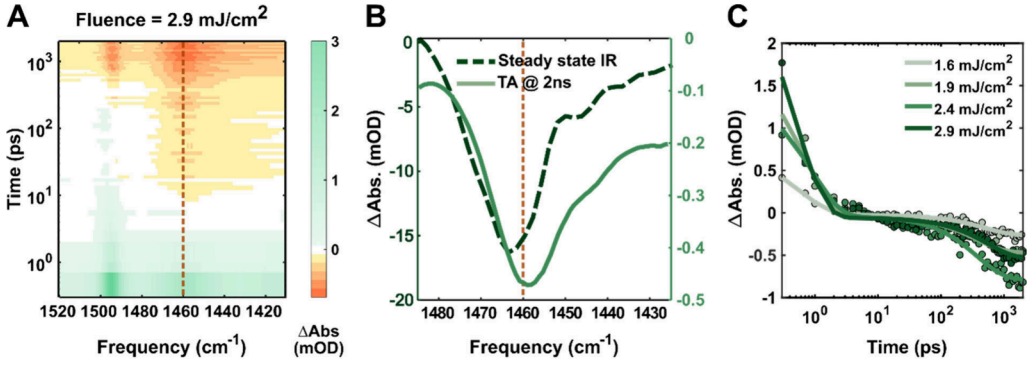

Figure 3. (A) MIR TA spectra of ITO NCs in toluene measured at a fluence of 2.9 mJ/cm^2. The dashed line highlights the growth of a negative signal that tracks photoinduced heating of toluene. (B) Comparison between a steady-state temperature difference spectrum constructed by subtracting an absorption spectrum measured at 25 °C from one measured at 30 °C (dashed dark green) and the TA spectrum measured at a time delay of 2 ns (solid green). (C) TA kinetic traces constructed by averaging TA spectra from 1450 to 1470 cm^{-1}. The solid lines represent biexponential fits whose parameters are given in Table 2. The transition from light to dark green represents increasing pump fluence.

https://doi.org/10.1021/acs.nanolett.5c02441
Nano Lett. XXXX, XXX, XXX−XXX

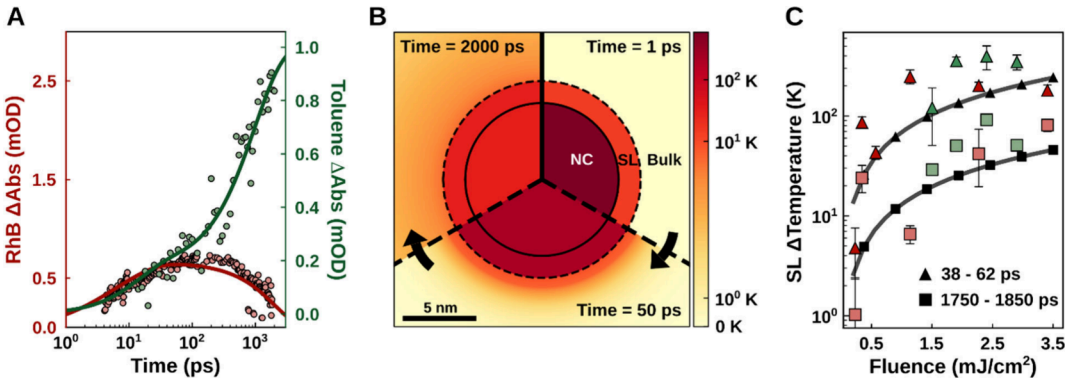

Figure 4. (A) Comparison of kinetics from TA experiments (points) and the theoretical heat transfer model (lines). The red and green points, respectively, represent the RhB PIA signal at 580 nm measured at a fluence of 2.3 mJ/cm^2 and the toluene TA signal averaged over 1450−1470 cm^{-1} at a fluence of 2.4 mJ/cm^2. Red and green lines show the modeled RhB and toluene signals, respectively, which were computed by converting the temperatures predicted with the thermal model into absorption changes as described in Sections S4.3-S4.4 of the Supporting Information. Arbitrary vertical scaling was applied to the temperature for each model curve to match the amplitude of its respective experiment. (B) The modeled photothermal heat dissipation of an oleate-capped ITO NC, its surrounding surface layer (SL), and the bulk solvent over time following NC photoexcitation. The bulk region is truncated to visually distinguish the NC and SL while preserving scale. The color bar denotes the temperature change from the system's initial temperature. (C) SL temperature change as a function of fluence averaged over two time windows: 38−62 ps (triangles) and 1750−1850 ps (squares). The two-interface model temperatures are shown in black, and the temperatures converted from experimental RhB and toluene TA signals are shown in red and green, respectively. Error bars are propagated from the signal standard deviation, averaging over the time window.

the bulk solvent occurs, thus marking the max temperature achieved by the SL. Subsequently, heat continues to transfer into the bulk solvent, extending beyond 2 ns. Note that the thermal model incorporates heat generation from neighboring NCs via zero-flux boundary conditions. The minimal temperature rise at the simulation boundary indicates heat contributions from neighboring NCs have a negligible impact on the overall heat dissipation.

By relating changes in absorption spectra of RhB and toluene to their temperature, we determine the SL temperature at selected experimental delay times as a function of fluence, which can be directly compared to the model (Figure 4C). The expected change in SL temperature from the model (black) and the values calculated from experimental TA signals of RhB (red) and toluene (green) are averaged over two time windows: 38−62 ps (triangles) and 1750−1850 ps (squares). The earlier window captures the period of maximum SL temperature rise while the latter represents the latest time window accessible in our TA experiments. Overall, the experimental and theoretical temperature profiles as a function of fluence show strong agreement, with predicted temperatures aligning well and exhibiting an increasing trend with higher fluence. This consistency further validates our theoretical model in accurately predicting the photothermal heat generation of oleate-capped ITO NCs in toluene.

Importantly, our combination of measurements and modeling indicates the SL temperature can reach values that are elevated by a few hundred Kelvin relative to the SL's initial temperature. This large temperature increase can persist for several hundred picoseconds due to the mismatch between G_{ls} and G_{sb}. Thus, ITO NCs may be well suited for applications wherein local heating of molecules at a NC's surface are required, such as driving catalytic reactions using heat and reshaping the local structure of temperature-sensitive NC assemblies.[35−38]

By combining experimental probes at the ITO NC surface and in the surrounding bulk solvent with a two-interface model, this study quantifies photothermal heat dissipation across the NC-SL-bulk-solvent interface of oleate-capped ITO NCs suspended in toluene. This was achieved by measuring photoinduced shifts in absorption spectra of two complementary temperature probes, RhB and toluene, present at the surface of ITO NCs and in their surrounding environment. We find the primary bottleneck to heat dissipation is the low thermal conductance between the SL and bulk solvent. This bottleneck leads to significant buildup of heat in the SL, which could be useful for applications wherein molecule heating at NC surfaces is the primary objective. The framework and insights established here lay the foundation for future investigations into how ligand chemistry and other factors influence photothermal heat dissipation, guiding the optimization of photothermal devices.

■ ASSOCIATED CONTENT

Supporting Information

The Supporting Information is available free of charge at https://pubs.acs.org/doi/10.1021/acs.nanolett.5c02441.

Detailed methods for the preparation of ITO NC solutions and thin films; Discussion of steady-state and time-resolved optical spectroscopy techniques used to characterize ITO NC samples and approaches used to fit transient kinetics captured in time-resolved measurements; Description of the two-interface model used to describe heat dissipation by ITO NCs to their environment (PDF)

■ AUTHOR INFORMATION

Corresponding Authors

Sean T. Roberts − *Department of Chemistry, The University of Texas at Austin, Austin, Texas 78712, United States;* orcid.org/0000-0002-3322-3687; Email: roberts@cm.utexas.edu

Carlos R. Baiz − *Department of Chemistry, The University of Texas at Austin, Austin, Texas 78712, United States;* orcid.org/0000-0003-0699-8468; Email: cbaiz@cm.utexas.edu

https://doi.org/10.1021/acs.nanolett.5c02441
Nano Lett. XXXX, XXX, XXX−XXX

Delia J. Milliron − *McKetta Department of Chemical Engineering, The University of Texas at Austin, Austin, Texas 78712, United States; Department of Chemistry, The University of Texas at Austin, Austin, Texas 78712, United States;* orcid.org/0000-0002-8737-451X; Email: milliron@che.utexas.edu

Thomas M. Truskett − *McKetta Department of Chemical Engineering and Department of Physics, The University of Texas at Austin, Austin, Texas 78712, United States;* orcid.org/0000-0002-6607-6468; Email: ttruskett@che.utexas.edu

Authors

Boxi Li − *Department of Chemistry, The University of Texas at Austin, Austin, Texas 78712, United States*

Xiaobing Chen − *Department of Chemistry, The University of Texas at Austin, Austin, Texas 78712, United States;* orcid.org/0000-0002-6107-1713

Tanner A. Wilcoxson − *McKetta Department of Chemical Engineering, The University of Texas at Austin, Austin, Texas 78712, United States*

Jiho Kang − *McKetta Department of Chemical Engineering, The University of Texas at Austin, Austin, Texas 78712, United States*

Complete contact information is available at: https://pubs.acs.org/10.1021/acs.nanolett.5c02441

Author Contributions

‖Boxi Li and Xiaobing Chen contributed equally to this work.

Author Contributions

S.T.R., C.R.B., D.J.M., and T.M.T. designed the study and secured funding. B.L. and X.C. conducted and analyzed the TA experiments and prepared the associated figures and text. T.A.W. performed theoretical modeling and prepared the corresponding figures and Supporting Information text. J.K. synthesized and characterized ITO NCs, prepared all samples, and measured their temperature-dependent absorption spectra. B.L. and X.C. drafted the manuscript, with all coauthors contributing to editing and revisions.

Notes

The authors declare no competing financial interest.

■ ACKNOWLEDGMENTS

This research was primarily supported by the National Science Foundation through the Center for Dynamics and Control of Materials: an NSF MRSEC under Cooperative Agreement No. DMR-2308817. Additional support was provided by the NSF through a DMREF grant (CBET-2323482), by the Army Research Office (Grant Number W911NF-23-1-0387), and by the Welch Foundation (F-1696 and F-1848). The authors also thank Prof. Gregory V. Hartland for helpful discussions.

■ REFERENCES

(1) Ben-Shahar, Y.; Scotognella, F.; Kriegel, I.; Moretti, L.; Cerullo, G.; Rabani, E.; Banin, U. Optimal Metal Domain Size for Photocatalysis with Hybrid Semiconductor-Metal Nanorods. *Nat. Commun.* **2016**, *7*, 10413.

(2) Kim, C.; Hyeon, S.; Lee, J.; Kim, W. D.; Lee, D. C.; Kim, J.; Lee, H. Energy-Efficient CO_2 Hydrogenation with Fast Response Using Photoexcitation of CO_2 Adsorbed on Metal Catalysts. *Nat. Commun.* **2018**, *9*, 3027.

(3) Yang, W.; Liu, Y.; McBride, J. R.; Lian, T. Ultrafast and Long-Lived Transient Heating of Surface Adsorbates on Plasmonic Semiconductor Nanocrystals. *Nano Lett.* **2021**, *21* (1), 453−461.

(4) Zhou, Z.; Kong, B.; Yu, C.; Shi, X.; Wang, M.; Liu, W.; Sun, Y.; Zhang, Y.; Yang, H.; Yang, S. Tungsten Oxide Nanorods: An Efficient Nanoplatform for Tumor CT Imaging and Photothermal Therapy. *Sci. Rep.* **2014**, *4*, 3653.

(5) Hessel, C. M.; Pattani, V. P.; Rasch, M.; Panthani, M. G.; Koo, B.; Tunnell, J. W.; Korgel, B. A. Copper Selenide Nanocrystals for Photothermal Therapy. *Nano Lett.* **2011**, *11* (6), 2560−2566.

(6) Tian, Q.; Jiang, F.; Zou, R.; Liu, Q.; Chen, Z.; Zhu, M.; Yang, S.; Wang, J.; Wang, J.; Hu, J. Hydrophilic Cu_9S_5 Nanocrystals: A Photothermal Agent with a 25.7% Heat Conversion Efficiency for Photothermal Ablation of Cancer Cells in Vivo. *ACS Nano* **2011**, *5* (12), 9761−9771.

(7) Li, K.; Zhang, Q.; Cui, X.; Liu, Y.; Liu, Y.; Yang, Y. Photothermal-Driven Soft Actuator Capable of Alternative Control Based on Coupled-Plasmonic Effect. *Chem. Eng. J.* **2024**, *498*, 155057.

(8) Elnaggar, A.; Kang, S.; Tian, M.; Han, B.; Keshavarz, M. State of the Art in Actuation of Micro/Nanorobots for Biomedical Applications. *Small Sci.* **2024**, *4* (3), 2300211.

(9) Kuppe, C.; Rusimova, K. R.; Ohnoutek, L.; Slavov, D.; Valev, V. K. "Hot" in Plasmonics: Temperature-Related Concepts and Applications of Metal Nanostructures. *Adv. Opt. Mater.* **2020**, *8* (1), 1901166.

(10) Segui Barragan, V.; Roman, B. J.; Shubert-Zuleta, S. A.; Berry, M. W.; Celio, H.; Milliron, D. J. Dipolar Ligands Tune Plasmonic Properties of Tin-Doped Indium Oxide Nanocrystals. *Nano Lett.* **2023**, *23* (17), 7983−7989.

(11) Ofosu, C. K.; Kang, J.; Truskett, T. M.; Milliron, D. J. Effective Hard-Sphere Repulsions between Oleate-Capped Colloidal Metal Oxide Nanocrystals. *J. Phys. Chem. Lett.* **2022**, *13* (48), 11323−11329.

(12) Shu, C.; Zhang, N.; Gao, Y.; An, J.; Wen, X.; Ma, W.; Liu, Z.; Sun, B.; Li, S. Multifunctional Sensors Based on Doped Indium Oxide Nanocrystals. *ACS Appl. Mater. Interfaces* **2022**, *14* (21), 24648−24658.

(13) Kriegel, I.; Scotognella, F.; Manna, L. Plasmonic Doped Semiconductor Nanocrystals: Properties, Fabrication, Applications and Perspectives. *Phys. Rep.* **2017**, *674*, 1−52.

(14) Indhu, A. R.; Keerthana, L.; Dharmalingam, G. Plasmonic Nanotechnology for Photothermal Applications − an Evaluation. *Beilstein J. Nanotechnol.* **2023**, *14* (1), 380−419.

(15) Baffou, G.; Quidant, R. Thermo-Plasmonics: Using Metallic Nanostructures as Nano-Sources of Heat. *Laser Photonics Rev.* **2013**, *7* (2), 171−187.

(16) Jauffred, L.; Samadi, A.; Klingberg, H.; Bendix, P. M.; Oddershede, L. B. Plasmonic Heating of Nanostructures. *Chem. Rev.* **2019**, *119* (13), 8087−8130.

(17) Das, U.; Biswas, R.; Mazumder, N. Elucidating Thermal Effects in Plasmonic Metal Nanostructures: A Tutorial Review. *Eur. Phys. J. Plus* **2022**, *137* (11), 1248.

(18) Link, S.; El-Sayed, M. A. Optical Properties and Ultrafast Dynamics of Metallic Nanocrystals. *Annu. Rev. Phys. Chem.* **2003**, *54*, 331−366.

(19) Hartland, G. V.; Besteiro, L. V.; Johns, P.; Govorov, A. O. What's so Hot about Electrons in Metal Nanoparticles? *ACS Energy Lett.* **2017**, *2* (7), 1641−1653.

(20) Brongersma, M. L.; Halas, N. J.; Nordlander, P. Plasmon-Induced Hot Carrier Science and Technology. *Nat. Nanotechnol.* **2015**, *10*, 25−34.

(21) Nguyen, S. C.; Zhang, Q.; Manthiram, K.; Ye, X.; Lomont, J. P.; Harris, C. B.; Weller, H.; Alivisatos, A. P. Study of Heat Transfer Dynamics from Gold Nanorods to the Environment via Time-Resolved Infrared Spectroscopy. *ACS Nano* **2016**, *10* (2), 2144−2151.

(22) Hogan, N. J.; Urban, A. S.; Ayala-Orozco, C.; Pimpinelli, A.; Nordlander, P.; Halas, N. J. Nanoparticles Heat through Light Localization. *Nano Lett.* **2014**, *14* (8), 4640−4645.

(23) Lounis, S. D.; Runnerstrom, E. L.; Llordés, A.; Milliron, D. J. Defect Chemistry and Plasmon Physics of Colloidal Metal Oxide Nanocrystals. *J. Phys. Chem. Lett.* **2014**, *5* (9), 1564−1574.
(24) Agrawal, A.; Kriegel, I.; Milliron, D. J. Shape-Dependent Field Enhancement and Plasmon Resonance of Oxide Nanocrystals. *J. Phys. Chem. C* **2015**, *119*, 6227−6238.
(25) Jain, P. K.; Qian, W.; El-Sayed, M. A. Ultrafast Electron Relaxation Dynamics in Coupled Metal Nanoparticles in Aggregates. *J. Phys. Chem. B* **2006**, *110* (1), 136−142.
(26) Chen, M.; He, Y.; Huang, J.; Zhu, J. Synthesis and Solar Photo-Thermal Conversion of Au, Ag, and Au-Ag Blended Plasmonic Nanoparticles. *Energy Convers. Manag.* **2016**, *127*, 293−300.
(27) Yeshchenko, O. A.; Bondarchuk, I. S.; Gurin, V. S.; Dmitruk, I. M.; Kotko, A. V. Temperature Dependence of the Surface Plasmon Resonance in Gold Nanoparticles. *Surf. Sci.* **2013**, *608*, 275−281.
(28) Cui, X.; Ruan, Q.; Zhuo, X.; Xia, X.; Hu, J.; Fu, R.; Li, Y.; Wang, J.; Xu, H. Photothermal Nanomaterials: A Powerful Light-to-Heat Converter. *Chem. Rev.* **2023**, *123* (11), 6891−6952.
(29) Wu, C.; Neuner III, B.; John, J.; Milder, A.; Zollars, B.; Savoy, S.; Shvets, G. Metamaterial-Based Integrated Plasmonic Absorber/Emitter for Solar Thermo-Photovoltaic Systems. *J. Opt.* **2012**, *14* (2), 024005.
(30) Yu, Y.; Williams, J. D.; Willets, K. A. Quantifying Photothermal Heating at Plasmonic Nanoparticles by Scanning Electrochemical Microscopy. *Faraday Discuss.* **2018**, *210*, 29−39.
(31) Liu, Z.; Zhong, Y.; Shafei, I.; Borman, R.; Jeong, S.; Chen, J.; Losovyj, Y.; Gao, X.; Li, N.; Du, Y.; Sarnello, E.; Li, T.; Su, D.; Ma, W.; Ye, X. Tuning Infrared Plasmon Resonances in Doped Metal-Oxide Nanocrystals through Cation-Exchange Reactions. *Nat. Commun.* **2019**, *10*, 1394.
(32) Jansons, A. W.; Hutchison, J. E. Continuous Growth of Metal Oxide Nanocrystals: Enhanced Control of Nanocrystal Size and Radial Dopant Distribution. *ACS Nano* **2016**, *10* (7), 6942−6951.
(33) Lounis, S. D.; Runnerstrom, E. L.; Bergerud, A.; Nordlund, D.; Milliron, D. J. Influence of Dopant Distribution on the Plasmonic Properties of Indium Tin Oxide Nanocrystals. *J. Am. Chem. Soc.* **2014**, *136* (19), 7110−7116.
(34) Li, Y.; Li, S.; Chen, D.; Kocoj, C. A.; Yang, A.; Diroll, B. T.; Guo, P. Mid-Infrared Photodetection with 2D Metal Halide Perovskites at Ambient Temperature. *Sci. Adv.* **2024**, *10* (5), eadk2778.
(35) Kang, J.; Valenzuela, S. A.; Lin, E. Y.; Dominguez, M. N.; Sherman, Z. M.; Truskett, T. M.; Anslyn, E. V.; Milliron, D. J. Colorimetric Quantification of Linking in Thermoreversible Nanocrystal Gel Assemblies. *Sci. Adv.* **2022**, *8* (7), eabm7364.
(36) Kang, J.; Sherman, Z. M.; Conrad, D. L.; Crory, H. S. N.; Dominguez, M. N.; Valenzuela, S. A.; Anslyn, E. V.; Truskett, T. M.; Milliron, D. J. Structural Control of Plasmon Resonance in Molecularly Linked Metal Oxide Nanocrystal Gel Assemblies. *ACS Nano* **2023**, *17* (23), 24218−24226.
(37) Rusch, P.; Zámbó, D.; Bigall, N. C. Control over Structure and Properties in Nanocrystal Aerogels at the Nano-, Micro-, and Macroscale. *Acc. Chem. Res.* **2020**, *53* (10), 2414−2424.
(38) Green, A. M.; Ofosu, C. K.; Kang, J.; Anslyn, E. V.; Truskett, T. M.; Milliron, D. J. Assembling Inorganic Nanocrystal Gels. *Nano Lett.* **2022**, *22* (4), 1457−1466.
(39) Blemker, M. A.; Gibbs, S. L.; Raulerson, E. K.; Milliron, D. J.; Roberts, S. T. Modulation of the Visible Absorption and Reflection Profiles of ITO Nanocrystal Thin Films by Plasmon Excitation. *ACS Photonics* **2020**, *7* (5), 1188−1196.
(40) Padalkar, M. V.; Pleshko, N. Wavelength-Dependent Penetration Depth of near Infrared Radiation into Cartilage. *Analyst* **2015**, *140* (7), 2093−2100.
(41) Chen, Y.; Wang, S.; Zhang, F. Near-Infrared Luminescence High-Contrast in Vivo Biomedical Imaging. *Nat. Rev. Bioeng.* **2023**, *1*, 60−78.
(42) Abb, M.; Wang, Y.; De Groot, C. H.; Muskens, O. L. Hotspot-Mediated Ultrafast Nonlinear Control of Multifrequency Plasmonic Nanoantennas. *Nat. Commun.* **2014**, *5*, 4869.
(43) Guo, P.; Schaller, R. D.; Ketterson, J. B.; Chang, R. P. H. Ultrafast Switching of Tunable Infrared Plasmons in Indium Tin Oxide Nanorod Arrays with Large Absolute Amplitude. *Nat. Photonics* **2016**, *10* (4), 267−273.
(44) Tice, D. B.; Li, S. Q.; Tagliazucchi, M.; Buchholz, D. B.; Weiss, E. A.; Chang, R. P. H. Ultrafast Modulation of the Plasma Frequency of Vertically Aligned Indium Tin Oxide Rods. *Nano Lett.* **2014**, *14* (3), 1120−1126.
(45) Johns, R. W.; Blemker, M. A.; Azzaro, M. S.; Heo, S.; Runnerstrom, E. L.; Milliron, D. J.; Roberts, S. T. Charge Carrier Concentration Dependence of Ultrafast Plasmonic Relaxation in Conducting Metal Oxide Nanocrystals. *J. Mater. Chem. C* **2017**, *5*, 5757−5763.
(46) Araya-Hermosilla, E.; Gabbani, A.; Mazzotta, A.; Ruggeri, M.; Orozco, F.; Cappello, V.; Gemmi, M.; Bose, R. K.; Picchioni, F.; Pineider, F.; Mattoli, V.; Pucci, A. Rapid Self-Healing in IR-Responsive Plasmonic Indium Tin Oxide/Polyketone Nanocomposites. *J. Mater. Chem. A* **2022**, *10* (24), 12957−12967.
(47) Mazzotta, A.; Gabbani, A.; Carlotti, M.; Ruggeri, M.; Fantechi, E.; Ottomaniello, A.; Pineider, F.; Pucci, A.; Mattoli, V. Invisible Thermoplasmonic Indium Tin Oxide Nanoparticle Ink for Anti-Counterfeiting Applications. *ACS Appl. Mater. Interfaces* **2022**, *14* (30), 35276−35286.
(48) Berquist, Z. J.; Turaczy, K. K.; Lenert, A. Plasmon-Enhanced Greenhouse Selectivity for High-Temperature Solar Thermal Energy Conversion. *ACS Nano* **2020**, *14* (10), 12605−12613.
(49) Russo, S. K.; Cisneros, L. C.; Reynolds, B. J.; Crane, M. J. Efficient Hot Thermal Carrier Transfer in Plasmonic Metal Oxide Nanocrystals. *ACS Nano* **2025**, *19* (24), 22468−22476.
(50) Liang, Y.; Diroll, B. T.; Wong, K.-L.; Harvey, S. M.; Wasielewski, M.; Ong, W.-L.; Schaller, R. D.; Malen, J. A. Differentiating Thermal Conductances at Semiconductor Nanocrystal/Ligand and Ligand/Solvent Interfaces in Colloidal Suspensions. *Nano Lett.* **2023**, *23* (9), 3687−3693.
(51) Jansons, A. W.; Hutchison, J. E. Continuous Growth of Metal Oxide Nanocrystals: Enhanced Control of Nanocrystal Size and Radial Dopant Distribution. *ACS Nano* **2016**, *10* (7), 6942−6951.
(52) Maher, R. C.; Cohen, L. F.; Gallop, J. C.; Le Ru, E. C.; Etchegoin, P. G. Temperature-Dependent Anti-Stokes/Stokes Ratios under Surface-Enhanced Raman Scattering Conditions. *J. Phys. Chem. B* **2006**, *110* (13), 6797−6803.
(53) Xie, Y.; Boggs, J. E. The Computed Force Constants and Vibrational Spectra of Toluene. *J. Comput. Chem.* **1986**, *7* (2), 158−164.
(54) Tasumi, M.; Urano, T.; Nakata, M. Some Thoughts on the Vibrational Modes of Toluene as a Typical Monosubstituted Benzene. *J. Mol. Struct.* **1986**, *146*, 383−396.
(55) Zhou, D.; Li, X.; Zhou, Q.; Zhu, H. Infrared Driven Hot Electron Generation and Transfer from Non-Noble Metal Plasmonic Nanocrystals. *Nat. Commun.* **2020**, *11*, 2944.
(56) Beaumont, P. C.; Johnson, D. G.; Parsons, B. J. Excited State and Free Radical Properties of Rhodamine Dyes in Aqueous Solution: A Laser Flash Photolysis and Pulse Radiolysis Study. *J. Photochem. Photobiol., A* **1997**, *107* (1), 175−183.
(57) Yi, J.; You, E.-M.; Ding, S.-Y.; Tian, Z.-Q. Unveiling the Molecule−Plasmon Interactions in Surface-Enhanced Infrared Absorption Spectroscopy. *Nat. Sci. Rev.* **2020**, *7* (7), 1228−1238.
(58) Li, J.; Li, J.; Xia, X.-H. Plasmon Enhanced IR Spectroelectrochemistry. *ACS Meas. Sci. Au* **2024**, *4* (6), 606−614.
(59) Yan, N.; Qiu, Y.; He, X.; Tang, X.; Hao, Q.; Chen, M. Plasmonic Enhanced Nanocrystal Infrared Photodetectors. *Materials* **2023**, *16* (8), 3216.
(60) Agrawal, A.; Singh, A.; Yazdi, S.; Singh, A.; Ong, G. K.; Bustillo, K.; Johns, R. W.; Ringe, E.; Milliron, D. J. Resonant Coupling between Molecular Vibrations and Localized Surface Plasmon Resonance of Faceted Metal Oxide Nanocrystals. *Nano Lett.* **2017**, *17* (4), 2611−2620.
(61) Chang, W. J.; Roman, B. J.; Green, A. M.; Truskett, T. M.; Milliron, D. J. Surface-Enhanced Infrared Absorption Spectroscopy by

https://doi.org/10.1021/acs.nanolett.5c02441
Nano Lett. XXXX, XXX, XXX−XXX

Resonant Vibrational Coupling with Plasmonic Metal Oxide Nanocrystals. *ACS Nano* **2024**, *18* (31), 20636−20647.
(62) Shavalier, S. A.; Gezelter, J. D. Heat Transfer in Gold Interfaces Capped with Thiolated Polyethylene Glycol: A Molecular Dynamics Study. *J. Phys. Chem. B* **2023**, *127* (47), 10215−10225.
(63) Kuang, S.; Gezelter, J. D. Simulating Interfacial Thermal Conductance at Metal-Solvent Interfaces: The Role of Chemical Capping Agents. *J. Phys. Chem. C* **2011**, *115* (45), 22475−22483.
(64) Stocker, K. M.; Gezelter, J. D. Simulations of Heat Conduction at Thiolate-Capped Gold Surfaces: The Role of Chain Length and Solvent Penetration. *J. Phys. Chem. C* **2013**, *117* (15), 7605−7612.
(65) Fan, H.; Wang, M.; Han, D.; Zhang, J.; Zhang, J.; Wang, X. Enhancement of Interfacial Thermal Transport between Metal and Organic Semiconductor Using Self-Assembled Monolayers with Different Terminal Groups. *J. Phys. Chem. C* **2020**, *124* (31), 16748−16757.
(66) Kikugawa, G.; Ohara, T.; Kawaguchi, T.; Torigoe, E.; Hagiwara, Y.; Matsumoto, Y. A Molecular Dynamics Study on Heat Transfer Characteristics at the Interfaces of Alkanethiolate Self-Assembled Monolayer and Organic Solvent. *J. Chem. Phys.* **2009**, *130* (7), 074706.
(67) Diroll, B. T.; Schaller, R. D. Experimental Measurement of Particle-to-Particle Heat Transfer in Nanoparticle Solids. *ACS Nano* **2025**, *19* (16), 15698−15706.
(68) Hung, S.-W.; Kikugawa, G.; Shiomi, J. Mechanism of Temperature Dependent Thermal Transport across the Interface between Self-Assembled Monolayer and Water. *J. Phys. Chem. C* **2016**, *120* (47), 26678−26685.
(69) Diroll, B. T.; Schaller, R. D. Heating and Cooling of Ligand-Coated Colloidal Nanocrystals in Solid Films and Solvent Matrices. *Nanoscale* **2019**, *11* (17), 8204−8209.
(70) Diroll, B. T.; Guo, P.; Schaller, R. D. Heat Transfer at Hybrid Interfaces: Interfacial Ligand-to-Nanocrystal Heating Monitored with Infrared Pump, Electronic Probe Spectroscopy. *Nano Lett.* **2018**, *18* (12), 7863−7869.

https://doi.org/10.1021/acs.nanolett.5c02441
Nano Lett. XXXX, XXX, XXX−XXX